Title

Projection-defined ventral tegmental area neurons exhibit distinct fentanyl-induced molecular and functional adaptations that differentially support drug-context associations

Authors

Annalisa Montemarano[1], Hajra Sohail[1], Logan D. Fox[1], Laura B. Murdaugh[1], Alexandria E. Ostman[1], Samiksha Pandey[1], Kyrsten Derr[1], Megan E. Fox[1,2,3]

1. Department of Anesthesiology and Perioperative Medicine, Pennsylvania State University College of Medicine, Hershey PA
2. Department of Neuroscience and Experimental Therapeutics, Pennsylvania State University College of Medicine, Hershey PA
3. Address correspondence to Megan E Fox

   500 University Drive

   C2850, MC #H187

   Hershey, PA 17033

   Tel:717-531-0003 x289635

   mfox@psu.edu

Abstract

Synthetic opioids like fentanyl are contributing to unprecedented overdose rates. Despite the abundance of fentanyl in the illicit drug supply, an understanding of fentanyl's effects on the brain remains lacking. The ventral tegmental area (VTA) is an important site of fentanyl's rewarding actions in the brain and sends diverse projections to several regions including the nucleus accumbens (NAc) and prefrontal cortex (PFC). Previous work shows downstream projection target influences baseline properties and opioid-induced neuroadaptations in VTA, but most work has focused on single neurotransmitter-defined cell types. Here, we investigate how projection-defined VTA neurons exhibit different responses to fentanyl independent of cell type. We use RNA sequencing to show that fentanyl induces discordant transcriptional adaptations in VTA neurons that project to NAc vs PFC. We then used fiber photometry and chemogenetics to characterize functional differences in fentanyl-related behavior. We found different timescales of activation between VTA-NAc and VTA-PFC during conditioned place preference that support distinct aspects of fentanyl-context association. Together, our data demonstrate that based on projection target alone, VTA neurons can undergo vastly different adaptations in response to fentanyl, providing new insight into VTA encoding of opioid behaviors.

INTRODUCTION

Opioid use disorder (OUD) is a chronic, relapsing condition that impacts millions of individuals. The rate of opioid overdose deaths in the U.S. has dramatically escalated to unprecedented numbers in recent years, primarily due to increased prevalence of potent synthetic opioids like fentanyl [1]. Fentanyl possesses unique pharmacological properties compared to other opioids: its high lipid solubility allows for rapid passage through the blood brain barrier [2], it exhibits unique binding interactions with the mu opioid receptor [3], and distinct receptor selectivity as compared to morphine [4]. Fentanyl exposure is associated with poorer treatment outcomes for OUD [5], necessitating novel advances in treatment for OUD cases that involve fentanyl. Despite the increased prevalence of fentanyl misuse, an understanding of the neuroadaptations resulting from fentanyl misuse remains lacking.

The ventral tegmental area (VTA) is a heterogenous midbrain structure important for opioid reward [6,7] and rodents will self-administer morphine or fentanyl intracranially into this region [8,9]. The VTA sends mostly non-overlapping projections to several nodes in the reward circuit, including the nucleus accumbens (NAc) and prefrontal cortex (PFC) [10]. While the dopaminergic subset of VTA neurons and their response to drug misuse have been extensively characterized, not all VTA dopamine neurons are functionally identical. Rather, they exhibit several distinct properties depending on their downstream projection target, including baseline electrophysiological differences [10,11], and different inputs from other brain regions [12,13]. In mouse, VTA dopamine neurons that project to PFC have higher membrane excitability and faster firing rate that those that project to NAc [10,14–16], and differential expression of molecular markers for dopamine neurons [10,17,18]. VTA dopamine neurons also exhibit different responses to opioids depending on their downstream projection target, including differential degree of recruitment by morphine and fentanyl [19], distinct morphine-induced morphological changes [20], and selective inhibition by kappa opioid agonists [21].

Along with dopamine neurons, the VTA contains other neuron subtypes capable of releasing glutamate, GABA, or a combination of these [22–24]. VTA projections contain different proportions of neurotransmitter subtype depending on the projection target [25,26]. Recent work indicates many behavioral functions classically attributed to VTA dopamine neurons can also be mediated by glutamate [27–30], GABA [31,32], and co-transmitting [33–35] neurons. These functions extend to opioid use, as non-dopaminergic VTA neurons express mu opioid receptors [36], participate in opioid seeking behaviors [37,38], and undergo diverse molecular

adaptations following fentanyl self-administration [23]. However, it remains unclear whether the projection-specific response to opioids exhibited by VTA dopamine neurons is also shared by other VTA neurons, since most prior characterizations of VTA circuit function is limited to dopaminergic neurons.

Given the vast heterogeneity in VTA cell types, characterizing VTA function by putative neurotransmitter identity can be limiting. There is significant overlap among neurotransmitter markers, since the rate limiting enzyme for dopamine synthesis, tyrosine hydroxylase (TH), can be expressed in VTA neurons that release glutamate [39] or GABA [40]. Similarly, many VTA neurons that express the vesicular glutamate transporter 2 (VGLUT2) also express the vesicular GABA transporter (VGAT) and as such release both glutamate and GABA [35,41]. Oftentimes, VTA neurons belonging to the same putative neurotransmitter type exhibit opposing activity: VTA dopamine neurons can be activated by both rewarding and aversive stimuli [42], and VTA glutamate neurons can elicit both reward and aversion [33]. Further, VTA glutamate and GABA projection neurons form both distal and local connections, suggesting that activity at one cell type is directly influencing activity at other VTA neurons [36]. VTA encoding of behavior may better defined by characteristics other than neurochemical profiles. This may be especially true in the context of opioid use, since opioids engage neuronal ensembles in the VTA that bypass neurotransmitter type [43,44]. A circuit-specific approach to understanding VTA function in opioid use can elucidate novel insights into VTA encoding of opioid behaviors.

In this study we sought to understand how cellularly heterogeneous VTA projections respond to fentanyl and differentially drive drug-context association. We used RNA sequencing to compare fentanyl-induced transcriptional adaptations in VTA neurons that project to either NAc core (VTA-NAc) or medial PFC (VTA-PFC) and identify discordance between projection neuron populations. We then used a combination of *in vivo* approaches to investigate VTA-NAc and VTA-PFC activity during fentanyl conditioned place preference (CPP). Using fiber photometry, we found both projections had increased calcium activity during fentanyl exposure, but exhibited temporally distinct calcium dynamics during entries to the fentanyl-paired context. Finally, chemogenetic inhibition of VTA-NAc vs VTA-PFC differentially impacted fentanyl place preference. These studies provide novel insight into the unique transcriptional and functional adaptations occurring in specific VTA projections in response to fentanyl.

MATERIALS AND METHODS

Experimental subjects

All procedures were approved by the Institutional Animal Care and Use Committee at the Pennsylvania State University College of Medicine (PSUCOM) and conducted in accordance with NIH guidelines for the use of laboratory animals. RiboTag mice on a C57BL/6J background were obtained from The Jackson Laboratory (B6J.129(Cg)-*Rpl22*$^{tm1.1Psam}$/SjJ; Jax strain #029977; RRID:IMSR_JAX:029977) and bred at PSUCOM. All mice were given food and water *ad libitum* and housed in the PSUCOM vivarium on a 12:12h light:dark cycle with lights on at 7:00. All mice were group housed in corncob bedding and provided with nestlets. After fiber optic implantations, mice were pair-housed across a perforated acrylic divider to prevent isolation stress. All experiments used mice of both sexes aged 8-10 weeks at the start of behavior.

Stereotaxic surgery

Adeno-associated viruses for Cre recombinase (AAVrg.hSyn.HI.eGFP-Cre.WPRE.SV40 or AAV9-CMV-PI-Cre), Cre-dependent GCaMP8s (AAV9-syn-FLEX-jGCaMP8s-WPRE), Cre-dependent Gi-coupled (AAV9-hSyn-DIO-hM4D(Gi)-mCherry) Designer Receptors Exclusively Activated by Designer Drugs (DREADDs), and Cre-dependent mCherry control (AAV9-hSyn-DIO-mCherry) were acquired from Addgene (viral preps #105540-AAVrg, 105537-AAV9, 162377-AAV9, 44362-AAV9, 50459-AAV9). Mice were anesthetized with 1-4% isoflurane gas in oxygen delivered at 1 liter/min, and affixed in a stereotaxic frame (Stoelting, Dale IL). Mice had a small burr hole made over target brain regions using the following coordinates (in mm, relative to bregma): NAc core (AP +1.6, ML +1.5, DV -4.4, 10° angle), mPFC (AP +1.7, ML +0.75, DV -2.5, 15° angle), VTA (AP -3.2, ML +1.0, DV -4.6, 7° angle). Viral vectors were delivered with Hamilton neurosyringes with 33-gauge needles at a rate of 100 nL/min for a total volume of 300 nL/virus, then needles were left in place for 5 min to minimize spread up the tract. For RNA sequencing experiments, AAVrg-hSyn-eGFP-Cre was infused bilaterally in NAc core or mPFC of RiboTag mice. For fiber photometry, AAV9-CMV-Cre was infused bilaterally in NAc core or mPFC of wildtype mice, 0.4 nL DIO-GCaMP was infused unilaterally in the right VTA (AP -3.2, ML +0.4, DV -4.2, 0° angle), two screws were fixed to the skull, then a fiber optic cannula (Thorlabs #CFM14L05) was implanted above the right VTA (DV -4.0) and fixed to the skull with C&B Metabond Adhesive Cement (Parkell #S380). For chemogenetic experiments, AAVrg-hSyn-eGFP-Cre was infused bilaterally in NAc core or mPFC of wildtype mice, and DIO-hM4Gi or DIO-mCherry was infused bilaterally in VTA.

Drugs

Fentanyl citrate (#22659) obtained from Cayman chemical (Ann Arbor, MI), and deschloroclozapine (#7193) obtained from Tocris Bioscience (Minneapolis, MN), were dissolved in sterile saline (0.9%).

Conditioned place preference

Conditioned place preference (CPP) was performed as previously described [45] in a three-chambered rectangular apparatus consisting of a neutral center compartment and two side compartments with different contextual cues, connected by automatic guillotine doors, and equipped with infrared photobeam detectors that track animal position and movement (ENV-3013, MED Associates). On the first day of testing (pre-test), mice underwent a 5 min habituation in the center compartment, after which the doors opened, and they freely explored the entire apparatus for 20 min. The least-preferred chamber was subsequently assigned as the fentanyl-paired chamber. Mice then underwent 3 consecutive days of conditioning. On conditioning days, mice received an i.p. injection of saline (10 mL/kg) and were confined to the saline-paired compartment for 20 min; 4 h later, they received an i.p. injection of fentanyl (0.2 mg/kg) and were confined to the fentanyl-paired compartment for 20 min. On the fifth day of testing (post-test), after 5 min habituation in the center, they freely explored the entire apparatus for 20 min. CPP score was calculated as the difference in seconds spent in the fentanyl-paired context during post-test vs pre-test. Locomotion was measured as movement counts in Med-PC V Software.

Fiber photometry

Three weeks after surgery, mice were habituated to a dummy headstage in their homecage (2-3 days, ~10 min/day). Changes in GCaMP8s fluorescence were acquired with a TeleFipho Wireless Fiber Photometry system (Amuza, San Diego, California) and synchronized to behavioral events with TTL pulses via an AD instruments Interface and Lab Chart Lightning software. Prior to the first behavioral test, a >10 minute recording was taken to confirm GCaMP expression. A >5 minute recording was taken immediately prior to each CPP session to minimize signal decay during testing. Recordings were taken for pre-test, post-test, and all conditioning sessions (470 nm LED @ ~30uW excitation power; 500-550 nm emission). After testing completed, mice were perfused and brains processed for immunostaining as described below to confirm viral expression and fiber placement.

Custom MATLAB scripts were made for processing & analysis of fiber photometry recordings. To process recordings, TTL timestamps were used to trim recordings from start to end, a double exponential fit of the signal was generated as a pseudoisobestic control for debleaching [46], and z-scored ΔF/F (zΔF/F) values were

generated. A z cutoff of 3x median absolute deviation was used for transient identification, and all transients must have been ≥0.3 seconds in duration, and ≥0.5 seconds from the previous transient. Due to recording errors during conditioning sessions, any mice that did not have all 6 conditioning recordings were excluded from analysis of conditioning data. For analysis of test days, zΔF/F values within a 4 second window surrounding transitions between regions were identified. A mouse must have stayed in a region for at least 2 seconds for the transition to be included. To control for behavioral differences among mice, only the first 15 transitions into each region were analyzed for each mouse, which was the minimum number of transitions observed among any mouse. To compare waveforms, we adapted the MATLAB script developed by Jean-Richard-dit-Bressel and colleagues to obtain bootstrapped 95% confidence intervals [47].

Chemogenetics

At least 14 days after stereotaxic surgery, mice underwent fentanyl CPP as described above. On the fifth day, mice received i.p. injection of saline (or DCZ) 20 min before the post-test. Four hours later, mice were injected with 0.1 mg/kg DCZ (or saline) 20 min before a second post-test [45]. After testing, mice were euthanized and a stereomicroscope equipped with a fluorescence adapter (NightSea, Hatfield PA) was used to confirm GFP-tagged Cre expression in projection targets and mCherry-tagged hM4Gi expression in VTA. Any mice that did not have a positive CPP score after vehicle injection were excluded from analysis.

Immunostaining

Mice were transcardially perfused with PBS and 4% paraformaldehyde. Brains were removed and post-fixed for 24hr, then sectioned to a thickness of 50 μm with a compresstome (Precisionary Instruments, Ashland MA.) Slices were washed with PBS and blocked for 30 min in in PBS with 3% normal donkey serum and 0.3% Triton X-100. Slices were incubated at 4ºC overnight in blocking buffer containing appropriate primary antibodies (1:1000, chicken anti-GFP, Aves Lab, Tigard, OR, #GFP-1020; 1:1000 rabbit anti-TH, Calbiochem #657012). Slices were washed 3 x 10 min with PBS, then incubated for 2h in PBS containing secondary antibodies (1:500, Goat anti-Chicken-FITC, Aves Lab, #F-1005; Donkey anti-Rabbit Alexa Fluor 594, Jackson Immuno, West Grove, PA, #711-585-152;). Slices were washed with PBS 3 x 10 min, counterstained with DAPI, mounted with Fluoromount-G (Southern Biotech, Birmingham, AL), and imaged on a laser-scanning confocal (Leica SP8) or epifluorescence microscope (Nikon Labophot2).

Cell counting

A subset of wildtype mice received stereotaxic surgery to express GCaMP in VTA-NAc or VTA-PFC neurons as described above, but did not receive a fiber optic cannula to avoid tissue damage artifacts. After >3 weeks, they were perfused and VTA slices were processed for immunostaining of GFP and TH as described above. Images of the right VTA were acquired using a laser-scanning confocal (Leica SP8). Three VTA images were pooled per mouse. TH expression was used to outline VTA boundaries, then two investigators independently counted the number of GCaMP-expressing neurons in VTA and how many co-localized with TH-positive cells to obtain percentage TH-positive GCaMP neurons in VTA. Percentages obtained by each investigator were within 6% difference from each other for the same image, then averaged together to obtain one percentage per image.

RNA Isolation & Sequencing

Mice were euthanized by cervical dislocation, and brains were rapidly removed and chilled in ice cold PBS. Cold brains were cut into 1 mm coronal sections using an aluminum brain matrix, and tissue punches containing total VTA were collected with 14-gauge needle, then snap-frozen on dry ice and stored at -80 until processing. Polyribosomes were immunoprecipitated as described previously [48,49]. Briefly, tissue punches (3 mice pooled per sample) were homogenized by douncing in 1 mL homogenization buffer, and 50µL supernatant saved as input. Remaining supernatant was incubated with 5 µl anti-HA antibody (BioLegend #901515) at 4ºC overnight with constant rotation. Samples were then incubated with 400 uL of protein A/G magnetic beads (Thermo Scientific #88803) overnight at 4ºC with constant rotation. Beads were washed in a magnetic rack with high-salt buffer. RNA was extracted using Trizol (Invitrogen) and the RNeasy Mini Kit with a DNAse step (Qiagen) from both immunoprecipitated and input samples by adding lysis buffer supplemented with beta mercaptoethanol and following the manufacturer's instructions (3-5 samples/sex/projection/drug, 102 total mice). RNA quality and concentration were assessed using an Agilent BioAnalyzer, and cDNA libraries were prepared by the Penn State College of Medicine Genome Sciences Core using the SMARTer Stranded Total RNA-Seq Kit v3 – Pico Input Mammalian (Takara Bio, San Jose, CA) according to the manufacturer's instructions. Libraries were quantified by qPCR prior to sequencing on an Illumina NovaSeq 6000 with an S2 flow cell, generating 50 base pair paired-end reads (average of ~70 million reads per sample). Raw data were demultiplexed using bcl2fastq (Illumina), and adapter trimming was performed after UMI extraction with UMI-tools [50]. Sequencing reads were aligned to the mouse reference genome (GRCm39, Ensembl release 2.7.1a) using STAR [51] with a maximum of two

mismatches allowed per read. Gene-level counts were obtained using featureCounts [52], with multi-mapping reads included, reads assigned to multiple overlapping features counted fractionally, and the feature with the largest overlap prioritized.

Differential Expression and Genome network analysis

We applied two strategies to characterize gene expression changes. First, we used limma [53] (lmFit) to fit log2 normalized read counts per million to a linear model and tested for effects of fentanyl in each projection target population with sexes combined. We conducted threshold free, rank-rank hypergeometric overlap analysis (RRHO) in R using the RRHO2 package [54]. Heatmaps were used to visualize regions of significant overlap in gene regulation across projection targets. Second, we characterized the effects of fentanyl on gene co-expression networks. As a starting point for the analysis, we used limma to select sets of genes that exhibited nominally-significant effect (p-value <0.05) of fentanyl, sex, or projection target. We then used weighted gene co-expression network analysis (WGCNA) to characterize co-expressed modules, separately within each projection target. Module detection was performed using the blockwiseModules() function with power = 8, corType = bioCor, networkType = signed, minModuleSize = 30, reassignThreshold = 0, mergeCutHeight = 0.25, minMEtoSTay = 0 and otherwise default parameters. We tested for differential expression of module eigengenes with limma, using posthoc contrasts to estimate effects of fentanyl while adjusting for sex differences separately in each target. Hub genes for each module were defined by calculating the Pearson correlation between the eigenene and each gene in the module.

Gene Ontology and transcription factor analysis

We performed Gene Ontology (GO) analysis using gprofiler2 [55] and queried over-represented GO terms in each WGCNA module using a Benjamini & Hochberg False Discovery Rate (FDR) correction of 0.05. To reduce redundancy and improve biological specificity during visualization, enriched Gene Ontology (GO) terms from g:Profiler analyses were filtered to remove broad parent categories. Terms with large gene sets (term size > 500) were excluded to avoid enrichment driven by highly general processes. We identified common transcriptional regulators of selected WGCNA modules using the iRegulon plug-in in Cytoscape [56] using program default settings.

RESULTS

Discordant fentanyl-induced transcriptional adaptations in VTA-NAc and VTA-PFC

Mesocortical and mesolimbic VTA neurons exhibit diverse morphologic adaptations and differential immediate early gene induction following chronic opioid exposure [19,20]. To examine if similar projection-specific adaptations occur at the transcriptional level, we used a retrograde Cre virus in either NAc core or PFC in Ribotag mice to tag ribosomes in specific VTA projection neurons (**Fig 1A**). Mice received one week of fentanyl injections, using a dose that produces physical dependence and can cause locomotor sensitization [57]. After 24h abstinence, we isolated and sequenced ribosome-associated RNA from VTA neurons projecting to either NAc or PFC, along with RNA from the input fraction representing total VTA. First, to confirm projection neuron enrichment of our samples, we compared expression of several cell-type markers in the immunoprecipitated samples relative to input in saline treated mice. We found significant enrichment of general neuronal markers (*Mapt*, *Tubb3*, *Map2*, *Nlgn3*, *Nefl, Eno2,* p's≤ 4.2×10^{-5}), and de-enrichment of markers for oligodendrotyces (*Aspa*), astrocytes (*Slc1a3*), microglia (*Arhgap15*), and pericytes (*Pla1a*, p's≤ 6.4×10^{-5}; **Fig 1B**). We next looked for enrichment of neuron subtype markers, and identified heterogeneity in both samples (**Fig 1B**): In VTA-PFC, we found significant enrichment of several monoaminergic, glutamatergic, and GABAergic markers; in VTA-NAc, we found enrichment of monoaminergic and glutamatergic markers, alongside *Crhbp*, which is enriched in co-transmitter populations [22,23]. In the VTA-NAc samples we also found enrichment of *Crhr1* and de-enrichment of *Cck* (0.47 vs -0.35 fold change, respectively), demonstrating our VTA-NAc population are primarily NAc core projecting neurons [58].

We next examined the top differentially expressed protein coding genes in the mesocortical vs mesolimbic populations as a consequence of fentanyl exposure and compared them with the top differentially expressed genes (DEGs) in total VTA (**Fig 1C,** all genes in **Supplemental File 1**). Strikingly, there was little concordance in the top 5 most up- and downregulated genes, with some genes showing opposite expression changes in the projection specific populations (e.g. *Gbx2* and *Lhx9* are downregulated in VTA-PFC and upregulated in VTA-NAc). The only statistically significant concordant gene was *Chrna2*, which demonstrated a similar degree of upregulation across the three populations. There was little overlap when extending the comparison to any DEG with $p<0.05$, with most showing expression changes in only one population (**Fig 1D**). Further, nearly twice as many genes were differentially expressed in VTA-PFC vs VTA-NAc (VTA-PFC: 1100

upregulated, 1071 downregulated; VTA-NAc: 379 upregulated, 592 downregulated; **Supplemental File 1**). To ensure the observed discordance was not driven by arbitrary p-value cutoffs, we next applied rank-rank hypergeometric overlap (RRHO) analysis. This threshold-free method assesses the significance of overlap between two gene lists ranked by their degree of differential expression rather than by p-value [54,59]. We first compared gene expression changes in input (total VTA) to either VTA-PFC or VTA-NAc after fentanyl and expected significant overlap as these projection populations are part of total VTA. For both comparisons we found significant overlap in the upper right and lower left quadrants, indicating concordance (**Fig 1E-G**), although the overlap between total VTA and VTA-PFC was greater relative to VTA-NAc. When comparing ranked gene lists between VTA-PFC and VTA-NAc, we found significant overlap in the upper left and lower right quadrants, revealing significant discordance (**Fig 1H**), confirming fentanyl dysregulated genes diverge between mesocortical and mesolimbic projection neurons regardless of p-value cutoffs.

To further characterize transcriptional adaptations in the mesocortical and mesolimbic neurons, we next performed weighted gene co-expression network analysis (WGCNA) separately in each projection neuron population. We identified 28 modules of co-expressed genes in VTA-PFC, and 14 in VTA-NAc with a $p<0.05$ effect of fentanyl in either sex, or with sexes combined (**Fig 1I-J, Supplemental File 1**). To define the functional enrichment within the fentanyl associated modules, we performed gene ontology (GO) analysis on the genes within each module (Top terms in **Fig 2A,C**, all enrichments in **Supplemental File 1**). Genes in upregulated VTA-PFC modules were enriched for neurotransmission related terms, such as neurotransmitter reuptake (P23), positive regulation of dopamine secretion (P64), and G protein activity (P66). Genes in downregulated VTA-PFC modules were also focused on neurotransmission, such as synaptic vesicle (P4), regulation of postsynaptic membrane potential (P17), and regulation of cytosolic calcium (P39; **Fig 2A**). Genes in upregulated VTA-NAc modules were enriched for several metabolic terms such as N-acylethanolamine metabolism (N39) and regulation of reactive oxygen species metabolism (N29), while genes in downregulated VTA-NAc modules were enriched for terms related to translation initiation (N28) and protein targeting to endoplasmic reticulum (N18; **Fig 2C**). We then visualized four gene networks per population, based on the top upregulated and downregulated eigengenes, along with an upregulated and downregulated module enriched for GO terms of interest (**Fig 2B,D**). We identified several different hub genes of interest in our selected modules: For VTA-PFC, these include upregulated phosphoinositide 3-kinase *Pik3c2b* (P43), vesicular monoamine transporter *Slc18a2* (P23), and

downregulated L-type calcium channel subunit Cacnb1 (P16) and calcium binding Calb2 (Calretinin; P4; **Fig 2B**). For VTA-NAc, these include upregulated acetylcholine receptor regulator *Lypd6b* (N39), upregulated transcription factors *Mef2c* and *Foxg1* (N29), and downregulated chromatin regulators *Mrbgp* (N21) and *Rbm14* (N18; **Fig 2D**).

Given the overrepresentation of transcription factors in VTA-NAc, we looked for additional transcriptional regulators of our select gene networks across projections with iRegulon [56] (top transcription factors for select modules in **Fig 2E,G,** all in **Supplemental File 1**). Informed by prior literature, we chose a transcription factor from each projection group previously implicated in substance use disorder [60,61] for visualization. For VTA-PFC, we chose Creb1, which was the top regulator for P43 (**Fig 2F**). While Creb1 itself was not changed, 19 of its target genes were upregulated as a function of fentanyl exposure. For VTA-NAc, we found that Mef2c, a N29 hub gene, was also the top regulator of N29 (**Fig 2H**).

Both VTA-NAc and VTA-PFC exhibit elevated calcium activity during fentanyl conditioning

Given the distinct transcriptional adaptations occurring in VTA-NAc and VTA-PFC in response to chronic fentanyl, we next asked whether these two neuronal populations exhibit different patterns of activity in response to fentanyl reward. We used fiber photometry to measure calcium activity of VTA-NAc and VTA-PFC during fentanyl conditioned place preference (**Fig 3A**). Like our RNA sequencing, we found heterogeneity in projection-specific cell types expressing GCaMP, with 32.5% of VTA-NAc GCaMP-expressing neurons, and 28.4% of VTA-PFC GCaMP-expressing neurons, colocalizing with TH (**Fig 3B**; n=5 mice per projection target group x 3 images per mouse; VTA-NAc vs VTA-PFC t-test, t_8=1.22, p=0.26). All mice spent more time in the fentanyl-paired context during the post-test compared to pre-test, and there were no significant behavioral differences between projection target groups (**Fig 3C**; session $F_{1,18}$=63.19, p<0.0001; projection target group $F_{1,18}$=0.30, p=0.59). To examine activity of VTA-NAc and VTA-PFC neurons in response to fentanyl we analyzed photometry data during the conditioning sessions (**Fig 3D**). There were no main effects of conditioning day, so data were averaged across days and analyzed with paired t-test. For both VTA-NAc and VTA-PFC neurons, we found a greater number of calcium transients during fentanyl conditioning relative to saline (VTA-NAc: **Fig 3E**, t_8=3.79, p=0.005; VTA-PFC: **Fig 3F**, t_5=4.04, p=0.0099) but no difference in average transient amplitude (VTA-NAc: t_8=0.68, p=0.52; VTA-PFC: t_5=1.45, p=0.21). We then analyzed transient frequency during the post-test and found signals resembling reward prediction error. VTA-NAc had reduced transient frequency when the mouse was in the

fentanyl-paired context compared to the saline-paired context (**Fig 3G**, t_9=2.32, p=0.046) and VTA-PFC had a trend towards decreased frequency in the fentanyl-paired context (**Fig 3H**, t_9=1.84, p=0.0995). There were no differences in transient amplitude in the saline- vs fentanyl-paired context for either projection group (VTA-NAc: t_9=0.93, p=0.38; VTA-PFC: t_9=0.006, p=0.995).

Distinct calcium dynamics of VTA-NAc and VTA-PFC during entries to the fentanyl-paired context

Next, we asked if VTA-NAc and VTA-PFC were differentially engaged during entry into the fentanyl-paired context on test days, as others have shown VTA calcium increases during entry to a cocaine-paired context [62]. To control for behavioral differences among mice, we only analyzed the first 15 transitions into each side of the chamber for each mouse. Using bootstrapped 95% confidence intervals [47], we identified significantly greater calcium activity in VTA-NAc in the one second immediately preceding entries to the fentanyl-paired chamber relative to saline (**Fig 4A,G**). In contrast, VTA-PFC peaked earlier at about 2 seconds prior to fentanyl-paired entry (**Fig 4C,H**). The increased calcium activity in VTA projections during entries to the fentanyl-paired context did not reflect exits from the saline-paired context, since there were no differences in the signal when aligned to region exits (**Fig 4A,C**). Importantly, we did not identify any signals consistent with extinction, as the increased activity preceding fentanyl-paired region entry was consistent throughout the session for both projections (**Fig 4B,D**). To ensure these effects were consistent across animals, for each animal we calculated the mean zΔF/F in 1 second bins preceding region entries (-2 to -1 seconds from entry, and -1 to 0 seconds from entry) and used paired t-tests to compare between saline- and fentanyl-paired entries. During the pre-test, there were no differences in the binned mean zΔF/F preceding region entries for both VTA-NAc (**Fig 4E**) and VTA-PFC (**Fig 4F**), ensuring that the increased activity observed during the post-test is due to context associations and not pre-existing biases. Similar to what we observed with bootstrapped confidence intervals, VTA-NAc mean zΔF/F was greater in the -1 to 0 sec from fentanyl-paired compared to saline-paired entries after conditioning (**Fig 4G**, t_9=2.39, p=0.041). For VTA-PFC, there was a trend towards greater mean zΔF/F during fentanyl-paired entries at both -2 to -1 sec (**Fig 4H**, left; t_9=2.23, p=0.052) and -1 to 0 sec (**Fig 4H**, right; t_9=1.98, p=0.079).

Chemogenetic inhibition of VTA-NAc vs VTA-PFC impact distinct processes in fentanyl conditioned place preference

Lastly, we used chemogenetic inhibition to determine whether the different activity of VTA-NAc vs VTA-PFC observed with fiber photometry contributes to different aspects of fentanyl place preference. We expressed

the inhibitory DREADD hM4Di, or an mCherry control, in either VTA-NAc or VTA-PFC. Using a counterbalanced, within-subject design, mice underwent two post-tests 4 hours apart, each preceded by an injection of either DCZ or vehicle (**Fig 5A**). Chemogenetic inhibition of VTA-NAc reduced time spent in the fentanyl-paired context (**Fig 5B**; virus x treatment $F_{1,21}$=5.04, p=0.036; Sidak's post hoc, vehicle vs DCZ: hM4Gi p=0.012, mCherry p=0.95). Importantly, reduced time spent in fentanyl paired chamber was not due to reduced number of entries (**Fig 5C**; virus x treatment $F_{1,21}$=2.39, p=0.14) or reduced locomotion (**Fig 5D**; virus x treatment $F_{1,21}$=2.74, p=0.11). In contrast, chemogenetic inhibition of VTA-PFC did not significantly alter time spent in the fentanyl-paired context (**Fig 5E**; virus x treatment $F_{1,20}$=3.17, p=0.093; Sidak's post hoc, vehicle vs DCZ: mCherry p=0.36, hM4Gi p=0.44). However, this manipulation did reduce number of entries to the fentanyl-paired context (**Fig 5F**; virus x treatment $F_{1,20}$=4.45, p=0.048; Sidak's post hoc, vehicle vs DCZ: mCherry p=0.84, hM4Gi p=0.046) and movement counts throughout the post-test (**Fig 5G**; virus x treatment $F_{1,20}$=7.42, p=0.013 Sidak's post hoc, vehicle vs DCZ: mCherry p=0.45, hM4Gi p=0.028).

DISCUSSION

In this study we demonstrated that fentanyl induces distinct molecular and functional adaptations in VTA neurons depending on their downstream projection target. We used RNA sequencing to show that chronic fentanyl induces remarkably discordant translatome profiles in VTA neurons that project to NAc vs PFC. We then demonstrated that the discordance in projection-specific molecular adaptations induced by fentanyl is functionally reflected in projection-specific encoding of fentanyl-associated behavior. We found VTA-NAc and VTA-PFC exhibit distinct signals during the expression of fentanyl-context associations, and that inhibiting either projection impacts different processes in the behavior. These experiments provide novel insight into the molecular and activity profiles of specific VTA projections in response to fentanyl, revealing new ways that VTA circuits shape opioid-associated behaviors.

Projection-specific VTA neurons undergo discordant fentanyl-induced molecular changes

To investigate fentanyl-induced molecular adaptations in specific VTA projections, we sequenced ribosome-associated RNA from VTA-NAc and VTA-PFC neurons after chronic fentanyl exposure and found robust discordance in differential gene expression between the projections. Given the projection-specific nature of VTA dopamine neuronal responses to opioids [19–21], it is perhaps unsurprising that the transcriptional

response to opioids is also influenced by projection target. Even the most upregulated and most downregulated genes differed between the projections (**Fig 1C**). While this revealed several genes with novel links to opioids (e.g. *Npvf*, *Gbx2*, *Prg4*), we also revealed several genes with prior implications for other misused drugs. Some examples include *Ttr*, which is upregulated in input and VTA-PFC in our dataset and in other parts of the brain after cocaine exposure [63,64]; *Slc13a4*, which is upregulated in input and VTA-PFC in our dataset and in PFC following cocaine self-administration [65]; and *Tcf19,* which is downregulated in VTA-PFC and VTA-NAc in our dataset and in PFC after chronic cocaine [66]. Since these genes are implicated across brain regions and with multiple substances, they make promising potential targets for future substance use research.

Other notable differences between the VTA projections investigated here include the number and function of genes impacted by fentanyl. VTA-PFC had double the number of genes with a significant effect of fentanyl compared to VTA-NAc. Gene ontology revealed that DEG function also varied between the projections. A notable GO term is “regulation of reactive oxygen species (ROS) metabolic processes,” representing N29. Opioids induce ROS-dependent DNA damage in PFC and NAc that potentiate heroin seeking behavior [67], but such a mechanism has not been explored in VTA. Another notable GO term is “NAE metabolic process,” representing N39. This refers to a key component of endocannabinoid signaling, which has a role in natural reward signaling through VTA-NAc [68] that may extend to opioid reward. *Naaa* is a notable gene upregulated gene in this GO term and a promising molecular target, as intra-VTA NAAA inhibition reduces alcohol motivation in rats [69] A noticeable difference in the VTA-PFC gene ontology compared to VTA-NAc is the prevalence of neuron-specific terms. Terms like “collagen fibril organization,” “extracellular matrix,” and “actin binding” appear across several upregulated VTA-PFC modules, reflecting upregulated structural plasticity. This is reminiscent of chronic morphine increasing soma size exclusively in VTA dopamine neurons that project to PFC [20] and increasing dendrite diameter of DA neurons in the parabrachial region of the VTA, where PFC-projecting neurons primarily reside [70]. Across downregulated VTA-PFC modules, several synaptic GO terms (synaptic vesicle, presynaptic active zone, presynaptic cytosol, axonogenesis, neuron projection terminus) indicate altered synaptic plasticity in this projection [7]. In VTA-PFC we also found “positive regulation of cytosolic calcium ion concentration” representing P39, and downregulation of the intracellular calcium regulator *Calb2*, reflecting altered neuronal excitability in this projection. Discordant transcriptional adaptations across projections likely contribute to

projection-specific roles in opioid-related behavior, but additional work is needed to test the causal role of individual genes in each projection.

We chose select gene modules for further visualization of the gene network and identification of transcriptional regulators, highlighting several potential projection-specific gene targets and their associated transcription factors targets. A notable hub gene is *Lypd6b*, which is upregulated in N39 and encodes a modulator of nicotinic acetylcholine receptors. The nicotinic acetylcholine receptor is significant as *Chrna2* is one of the few upregulated genes shared across all VTA populations in our study. Nicotinic acetylcholine receptors are expressed on all VTA neuron subtypes [71], and its activity is necessary for morphine CPP [72]. Cholinergic inputs to VTA may serve to further distinguish functionally distinct VTA projections, as mesolimbic dopamine neurons are selectively excited by specific cholinergic inputs [73]. Another notable hub gene is *Mef2c*, which is upregulated in N29 and was also identified as one of the top transcriptional regulators of N29. *Mef2c*, encoding myocyte enhancer factor 2C, has been implicated as an addiction-relevant transcription factor [60,61], mainly for its role in regulating structural plasticity in the NAc that promotes the behavioral response to cocaine [74,75], but a connection to opioid actions in the VTA has not been previously identified. In VTA-PFC we found a different transcription factor, *Creb1*, encoding cAMP responsive element binding protein 1 that has also been extensively implicated across misuse of several substances including cocaine [76,77], nicotine [78], alcohol [79], and morphine [80–82]. While there has been significant focus on CREB function in NAc and locus coeruleus [60,61], its role in VTA warrants further investigation.

Projection-specific VTA neurons encode functionally distinct processes in fentanyl CPP

Given the extensive discordance in fentanyl-induced transcriptional adaptations between VTA projections, we sought to understand whether this extends to different functions in fentanyl-associated behaviors. We chose a fentanyl CPP paradigm because it is multifaceted (direct fentanyl exposure and fentanyl-context associations), robust (>95% of mice developed a preference for the fentanyl-paired context), and allows for within-subject comparisons (fentanyl vs saline, repeated preference testing). VTA activity is essential for CPP, since the VTA exhibits increased activity during entries to a cocaine-paired context [62] and VTA inactivation inhibits the expression of cocaine CPP [84]. While much prior work has characterized dopamine actions in CPP [84–86], dopamine is not necessarily essential for CPP, since dopamine deficient mice can form place

preferences for cocaine and morphine [87,88]. Therefore, a novel approach to investigating VTA function in CPP improves our understanding of how drug-context associations are formed.

In the present study we found both VTA-NAc and VTA-PFC increased activity during fentanyl exposure, consistent with classic opioid-mediated disinhibition in the VTA. After conditioning, VTA-PFC activity increased early in the transition to the fentanyl-paired context, potentially reflecting a decision-making process. In contrast, VTA-NAc activity peaks later in the transition, likely a response to reward-associated contextual cues, and exhibited decreased transient frequency when mice are in their fentanyl-paired context, reminiscent of a reward prediction error signal. Although both projections signal the place preference, they likely reflect distinct and unconnected processes, because inhibiting each of the projections impacted different aspects of the behavior. Chemogenetic inhibition of VTA-NAc reduced the amount of time that mice spent in the fentanyl-paired context, suggesting that this projection encodes the value of the fentanyl-paired context. In contrast, while chemogenetic inhibition of VTA-PFC did not affect overall time spent in the fentanyl-paired context, it did reduce both the number of entries to the fentanyl-paired context and movement counts, supporting a role for VTA-PFC in the initial decision to go to the fentanyl-paired context.

An important consideration is the heterogeneity in the neurotransmitter profiles of the VTA projections represented in this study. Our cell-type characterizations reveal we serendipitously overrepresented the non-dopaminergic proportion of VTA projections. Our immunolabelling revealed about 30% of GCaMP-expressing neurons were TH-positive in both projections. The proportion of TH+ VTA projection neurons varies with the method used. For example, retrograde tracers like Fluorogold reveal around 70% of mouse VTA projection neurons are TH+ [25], while Cre-expressing canine adenoviruses show more TH+ VTA-NAc (60%) than VTA-PFC (40%) [12]. Unexpectedly, in our RNA sequencing experiments, we found that VTA-NAc had lower enrichment of several dopaminergic markers compared to VTA-PFC (**Fig 1B**). We suspect this reflects differences in AAV transduction efficiency and not a true difference in the proportion of dopaminergic cell types between the projections. Indeed, others have shown that midbrain dopamine neurons are not efficiently captured by most AAV serotypes [83], and while different baseline properties of dopaminergic neurons across projections may influence their intrinsic tropism for AAVs, this requires further investigation. Despite a limited number of TH-expressing neurons, our experiments support functions often attributed to dopamine neurons can also be mediated by other VTA neurons.

Conclusions

Here we demonstrate distinct properties of projection-defined VTA neurons across multiple fentanyl modalities. Depending on their downstream projection target, VTA neurons adopt different fentanyl-induced translatome profiles and fentanyl-associated activity profiles. We identified several promising candidate genes and transcription factors, some novel and some with prior brain-wide implications for substance use disorders. We also elucidated how projection-specific VTA populations encode fentanyl-context associations independent of neurotransmitter identity, providing a previously under-appreciated viewpoint of VTA representations of opioid behaviors. These findings provide necessary insight to the circuit-level neuroadaptations resulting from fentanyl, thus improving our understanding of potential neural mechanisms underlying OUD.

Acknowledgements

The authors thank the Penn State College of Medicine Genome Sciences Core (RRID:SCR_021123) and Advanced Light Microscopy Core (RRID:SCR_022526).

Author Contributions

AM and MEF designed the experiments. AM, HS, LDF, LBM, AEO, and SP performed behavior experiments. MEF performed RNA isolation. AM and KD counted cells. AM, HS, and MEF performed data analysis. AM and MEF wrote the manuscript and prepared the figures with input from all authors.

Funding

This work was supported by NIH grant DA058661 awarded to MEF.

Competing Interests

The authors have nothing to disclose.

Data and code availability

RNAseq data have been deposited at GEO and are publicly available as of the date of publication. Differential expression, WGCNA, and all code are available at github.com/mfoxlab

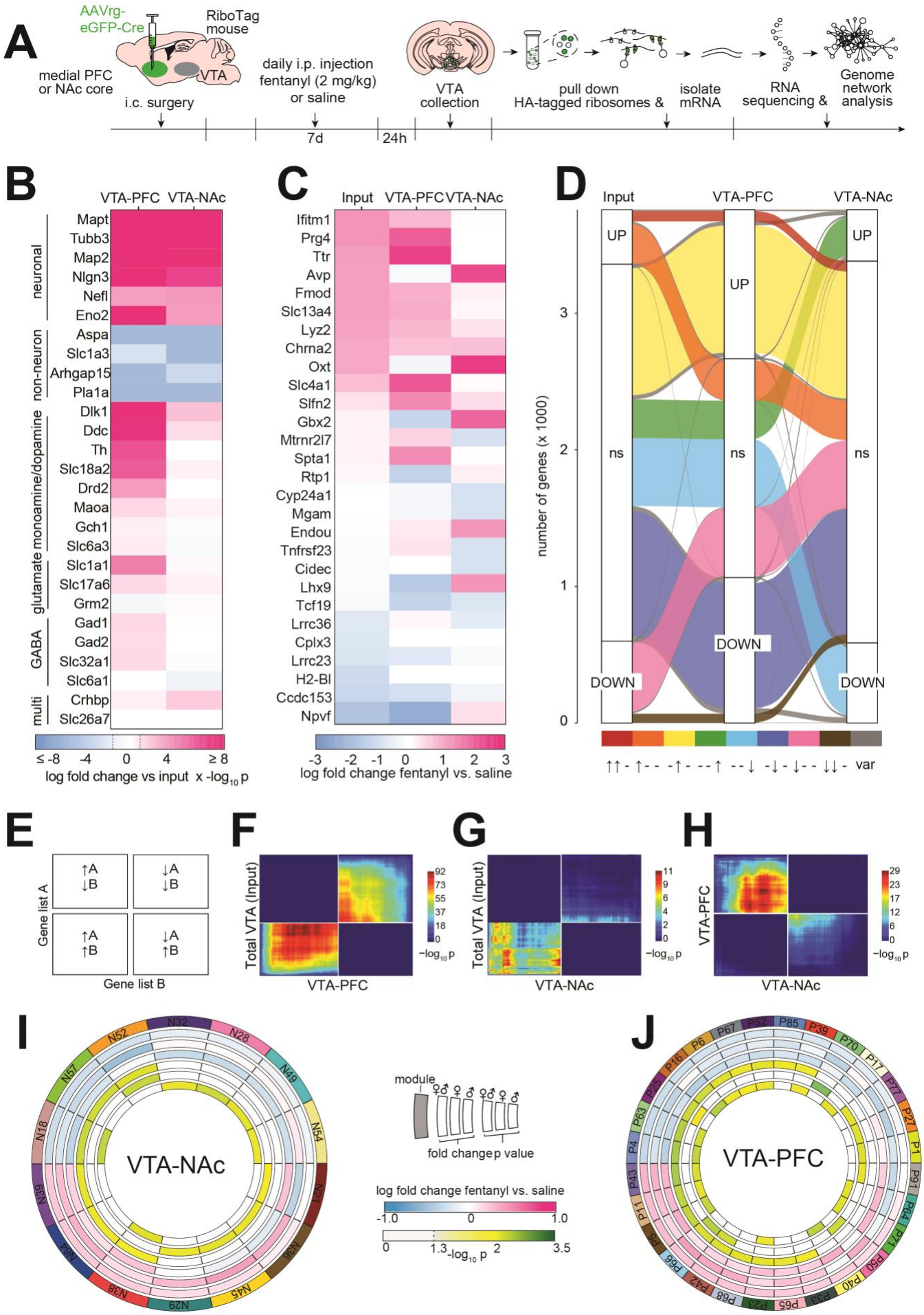
A
AAVrg-eGFP-Cre
RiboTag mouse
medial PFC or NAc core
VTA
i.c. surgery
daily i.p. injection fentanyl (2 mg/kg) or saline
7d
24h
VTA collection
pull down HA-tagged ribosomes &
isolate mRNA
RNA sequencing &
Genome network analysis
B
VTA-PFC VTA-NAc
neuronal
non-neuron
monoamine/dopamine
glutamate
GABA
multi
Mapt
Tubb3
Map2
Nlgn3
Nefl
Eno2
Aspa
Slc1a3
Arhgap15
Pla1a
Dlk1
Ddc
Th
Slc18a2
Drd2
Maoa
Gch1
Slc6a3
Slc1a1
Slc17a6
Grm2
Gad1
Gad2
Slc32a1
Slc6a1
Crhbp
Slc26a7
≤ -8 -4 0 4 ≥ 8
log fold change vs input x -log10 p
C
Input VTA-PFC VTA-NAc
Ifitm1
Prg4
Ttr
Avp
Fmod
Slc13a4
Lyz2
Chrna2
Oxt
Slc4a1
Slfn2
Gbx2
Mtrnr2l7
Spta1
Rtp1
Cyp24a1
Mgam
Endou
Tnfrsf23
Cidec
Lhx9
Tcf19
Lrrc36
Cplx3
Lrrc23
H2-Bl
Ccdc153
Npvf
-3 -2 -1 0 1 2 3
log fold change fentanyl vs. saline
D
Input VTA-PFC VTA-NAc
number of genes (x 1000)
UP
ns
DOWN
↑↑ - ↑- - -↑- - -↑ - -↓ -↓- ↓- - ↓↓ - var
E
Gene list A
Gene list B
↑A ↓B
↓A ↓B
↑A ↑B
↓A ↑B
F
Total VTA (Input)
VTA-PFC
92 73 55 37 18 0
−log10 p
G
Total VTA (Input)
VTA-NAc
11 9 6 4 2 0
−log10 p
H
VTA-PFC
VTA-NAc
29 23 17 12 6 0
−log10 p
I
VTA-NAc
N32 N28 N49 N54 N21 N36 N45 N29 N38 N54 N39 N18 N57 N52
module
fold change p value
log fold change fentanyl vs. saline
-1.0 0 1.0
0 1.3 -log10 p 2 3.5
J
VTA-PFC
P52 P85 P39 P70 P17 P77 P27 P1 P91 P64 P71 P50 P40 P33 P65 P23 P68 P42 P66 P5 P11 P43 P4 P63 P25 P16 P6 P67

Figure 1. **Chronic fentanyl induces discordant transcriptional adaptations between VTA-NAc and VTA-PFC neurons.** (**A**) Timeline for projection-specific VTA RNA sequencing experiments. Ribotag mice received retrograde Cre in either medial PFC or NAc core. Two weeks later, mice received 7 daily i.p. injections of 2 mg/kg fentanyl or equivalent volume of saline. Twenty-four hours after the last injection, brains were collected and fresh tissue punches containing VTA were flash frozen. Ribosome-associated RNA from VTA samples was isolated and prepared for RNA sequencing. (**B**) Heatmaps showing enrichment for neuron subtype markers and de-enrichment of non-neuronal markers in VTA-PFC or VTA-NAc saline samples vs saline input samples. (**C**) Heatmaps showing top five DEGs in fentanyl vs saline ($p<0.05$) across input, VTA-PFC, and VTA-NAc samples. (**C)** Alluvial plot comparing DEGs between neuronal populations. Combinations of upregulated (up), downregulated (down), and not significant (ns) genes are represented by individual colors. The 8 combinations with the most genes are colored, and the remaining combinations are represented in gray (**E**) RRHO interpretation schematic. (**F**) RRHO plots showing concordance of fentanyl-induced DEGs between total VTA and VTA-PFC, (**G**) concordance between total VTA and VTA-NAc, and (**H**) discordance between VTA-PFC and VTA-NAc, with $-\log_{10}$(P value) encoded in color using the adjacent color bars. (**I**) Circos plot showing WGCNA modules in VTA-NAc and (**J**) VTA-PFC pertaining to fentanyl, defined as differential eigengene expression with $p<0.05$ effect of fentanyl. Outer ring indicates an individual module assigned an arbitrary color and number. Fold change in eigengene expression and $-\log_{10}$(P value) are shown internally as sexes combined, then separately in females, and males, respectively. Hashed line on color bars indicates $p<0.05$ cut-offs.

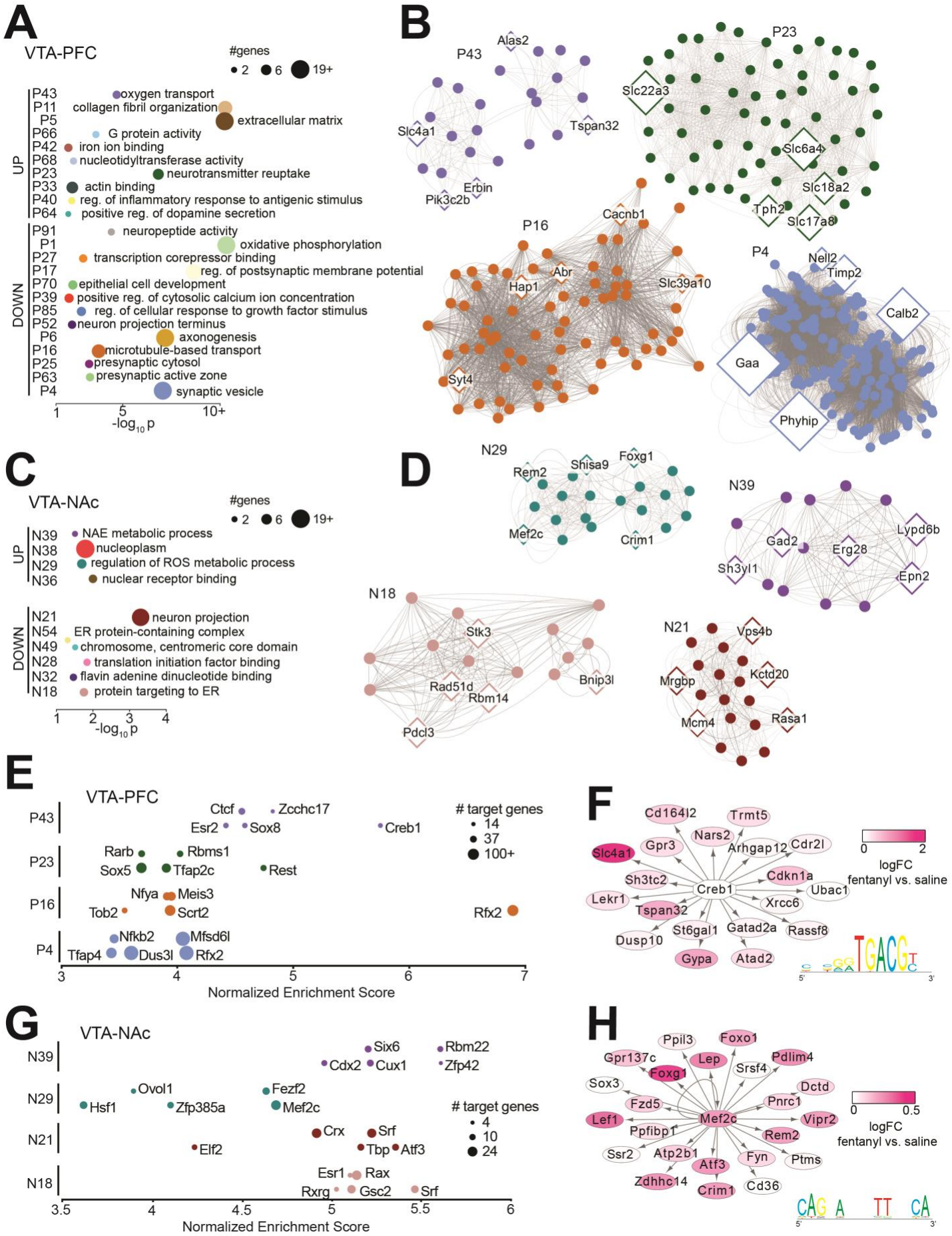
A
VTA-PFC
#genes
2
6
19+
UP
DOWN
P43 oxygen transport
P11 collagen fibril organization
P5 extracellular matrix
P66 G protein activity
P42 iron ion binding
P68 nucleotidyltransferase activity
P23 neurotransmitter reuptake
P33 actin binding
P40 reg. of inflammatory response to antigenic stimulus
P64 positive reg. of dopamine secretion
P91 neuropeptide activity
P1 oxidative phosphorylation
P27 transcription corepressor binding
P17 reg. of postsynaptic membrane potential
P70 epithelial cell development
P39 positive reg. of cytosolic calcium ion concentration
P85 reg. of cellular response to growth factor stimulus
P52 neuron projection terminus
P6 axonogenesis
P16 microtubule-based transport
P25 presynaptic cytosol
P63 presynaptic active zone
P4 synaptic vesicle
1
5
10+
-log10 p
B
P43
Alas2
Slc4a1
Tspan32
Erbin
Pik3c2b
P23
Slc22a3
Slc6a4
Slc18a2
Tph2
Slc17a8
P16
Cacnb1
Abr
Hap1
Slc39a10
Syt4
P4
Nell2
Timp2
Calb2
Gaa
Phyhip
C
VTA-NAc
#genes
2
6
19+
UP
DOWN
N39 NAE metabolic process
N38 nucleoplasm
N29 regulation of ROS metabolic process
N36 nuclear receptor binding
N21 neuron projection
N54 ER protein-containing complex
N49 chromosome, centromeric core domain
N28 translation initiation factor binding
N32 flavin adenine dinucleotide binding
N18 protein targeting to ER
1
2
3
4
-log10 p
D
N29
Rem2
Shisa9
Foxg1
Mef2c
Crim1
N39
Gad2
Erg28
Lypd6b
Sh3yl1
Epn2
N18
Stk3
Rad51d
Rbm14
Bnip3l
Pdcl3
N21
Vps4b
Mrgbp
Kctd20
Mcm4
Rasa1
E
VTA-PFC
P43
Ctcf
Zcchc17
Esr2
Sox8
Creb1
P23
Rarb
Rbms1
Sox5
Tfap2c
Rest
P16
Nfya
Meis3
Tob2
Scrt2
Rfx2
P4
Nfkb2
Mfsd6l
Tfap4
Dus3l
Rfx2
target genes
14
37
100+
3
4
5
6
7
Normalized Enrichment Score
F
Cd164l2
Trmt5
Nars2
Gpr3
Arhgap12
Cdr2l
Slc4a1
Sh3tc2
Cdkn1a
Creb1
Ubac1
Lekr1
Xrcc6
Tspan32
Dusp10
St6gal1
Gatad2a
Rassf8
Gypa
Atad2
0
2
logFC
fentanyl vs. saline
5'
3'
G
VTA-NAc
N39
Six6
Rbm22
Cdx2
Cux1
Zfp42
N29
Ovol1
Fezf2
Hsf1
Zfp385a
Mef2c
N21
Crx
Srf
Elf2
Tbp
Atf3
N18
Esr1
Rax
Rxrg
Gsc2
Srf
target genes
4
10
24
3.5
4
4.5
5
5.5
6
Normalized Enrichment Score
H
Ppil3
Foxo1
Gpr137c
Lep
Pdlim4
Foxg1
Srsf4
Sox3
Dctd
Fzd5
Pnrc1
Lef1
Mef2c
Vipr2
Ppfibp1
Rem2
Ssr2
Atp2b1
Fyn
Ptms
Atf3
Zdhhc14
Crim1
Cd36
0
0.5
logFC
fentanyl vs. saline
5'
3'

Figure 2. DEG function and transcriptional regulators vary between VTA-NAc and VTA-PFC. (**A**) Gene ontology analysis of VTA-PFC fentanyl modules. Modules are sorted by upregulated (UP) vs downregulated (DOWN). Circle size represents number of genes in the module enriched for the GO term listed to the right. One significant GO term was chosen to represent each module. (**B**) Gene networks for select VTA-PFC fentanyl modules. Genes with the most connections (hub genes) are labelled and indicated by diamonds, with the size of the diamond scaled to the number of connections. (**C**) Gene ontology analysis of VTA-NAc fentanyl modules. (**D**) Gene networks for select VTA-NAc modules. (**E**) The top 5 predicted transcriptional regulators identified for select VTA-PFC fentanyl modules. Circle size represents the number of genes in the module that are regulated by the labeled transcription factor. (**F**) Regulatory network for *Creb1*, a transcriptional regulator of P43. Arrows point to genes from P43 that are regulatory targets of *Creb1*. The log fold change for each gene is represented in color. A representative enriched binding motif for *Creb1* is below. (**G**) The top 5 transcriptional regulators identified for select VTA-NAc fentanyl modules. (**H**) Regulatory network for *Mef2c*, a transcriptional regulator of N29, and representative binding motif is below.

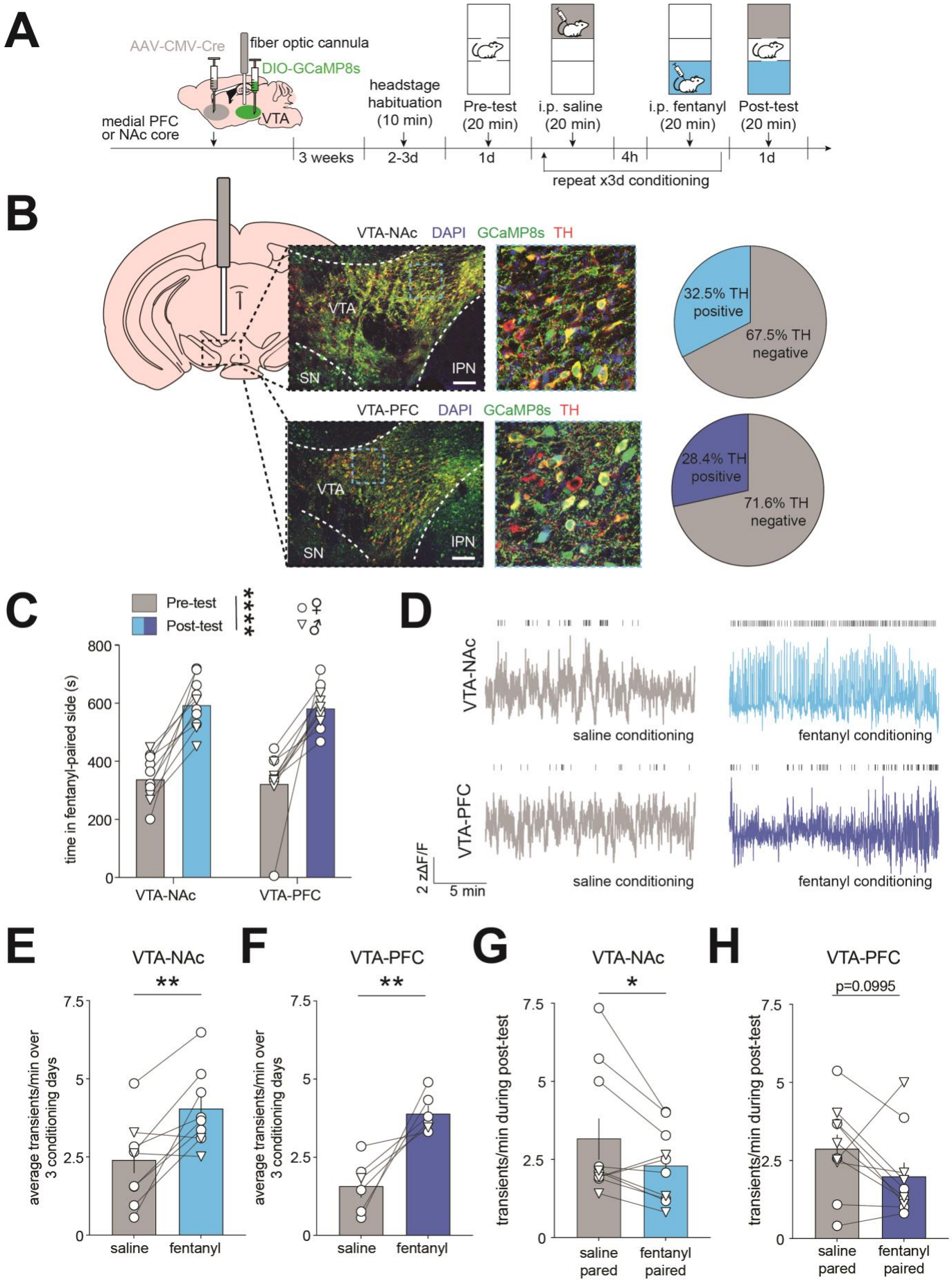
A
AAV-CMV-Cre
fiber optic cannula
DIO-GCaMP8s
medial PFC
or NAc core
VTA
headstage
habituation
(10 min)
Pre-test
(20 min)
i.p. saline
(20 min)
i.p. fentanyl
(20 min)
Post-test
(20 min)
3 weeks
2-3d
1d
4h
1d
repeat x3d conditioning
B
VTA-NAc DAPI GCaMP8s TH
VTA
SN
IPN
32.5% TH positive
67.5% TH negative
VTA-PFC DAPI GCaMP8s TH
28.4% TH positive
71.6% TH negative
C
Pre-test
Post-test
****
time in fentanyl-paired side (s)
VTA-NAc
VTA-PFC
D
VTA-NAc
VTA-PFC
saline conditioning
fentanyl conditioning
2 zΔF/F
5 min
E
VTA-NAc
average transients/min over 3 conditioning days
saline
fentanyl
F
VTA-PFC
G
VTA-NAc
transients/min during post-test
saline pared
fentanyl paired
H
VTA-PFC
p=0.0995

Figure 3. VTA-NAc and VTA-PFC have elevated calcium activity in response to fentanyl exposure. (**A**) Timeline for projection-specific VTA GCaMP fiber photometry experiments. Mice received retrograde Cre in either the medial PFC or NAc core, and Cre-dependent GCaMP8s in VTA, with a fiber optic cannula implanted directly above VTA. Three weeks later, mice underwent fentanyl CPP and VTA GCaMP activity was recorded during all sessions. (**B**) Representative images depicting GCaMP expression in VTA-NAc and VTA-PFC with immunostaining for TH. Approximately 32.5% of VTA-NAc GCaMP neurons, and 28.4% of VTA-PFC GCaMP neurons, were TH positive (n=5 mice per group). (**C**) All mice spent more time in the fentanyl-paired context during the post-test compared to pre-test (n=10 mice per group; main effect of session, ****, $p<0.0001$) (**D**) Representative calcium traces from VTA-NAc (top) and VTA-PFC (bottom) during saline conditioning (left) and fentanyl conditioning (right). Ticks above the trace indicate identified calcium transients. (**E**) In VTA-NAc, fentanyl increases transient frequency (n=9, average over 3 conditioning days, **, $p=0.005$) (**F**) In VTA-PFC, fentanyl increases transient frequency (n=6, average over 3 conditioning days, **, $p=0.0099$). (**G**) During the post-test, VTA-NAc has reduced transient frequency when the mouse is in the fentanyl-paired compared to saline-paired context (n=10; *, $p=0.046$) (**H**) No difference in VTA-PFC transient frequency in saline-paired vs fentanyl-paired context (n=10). Circles represent data points from females, triangles represent data points from males.

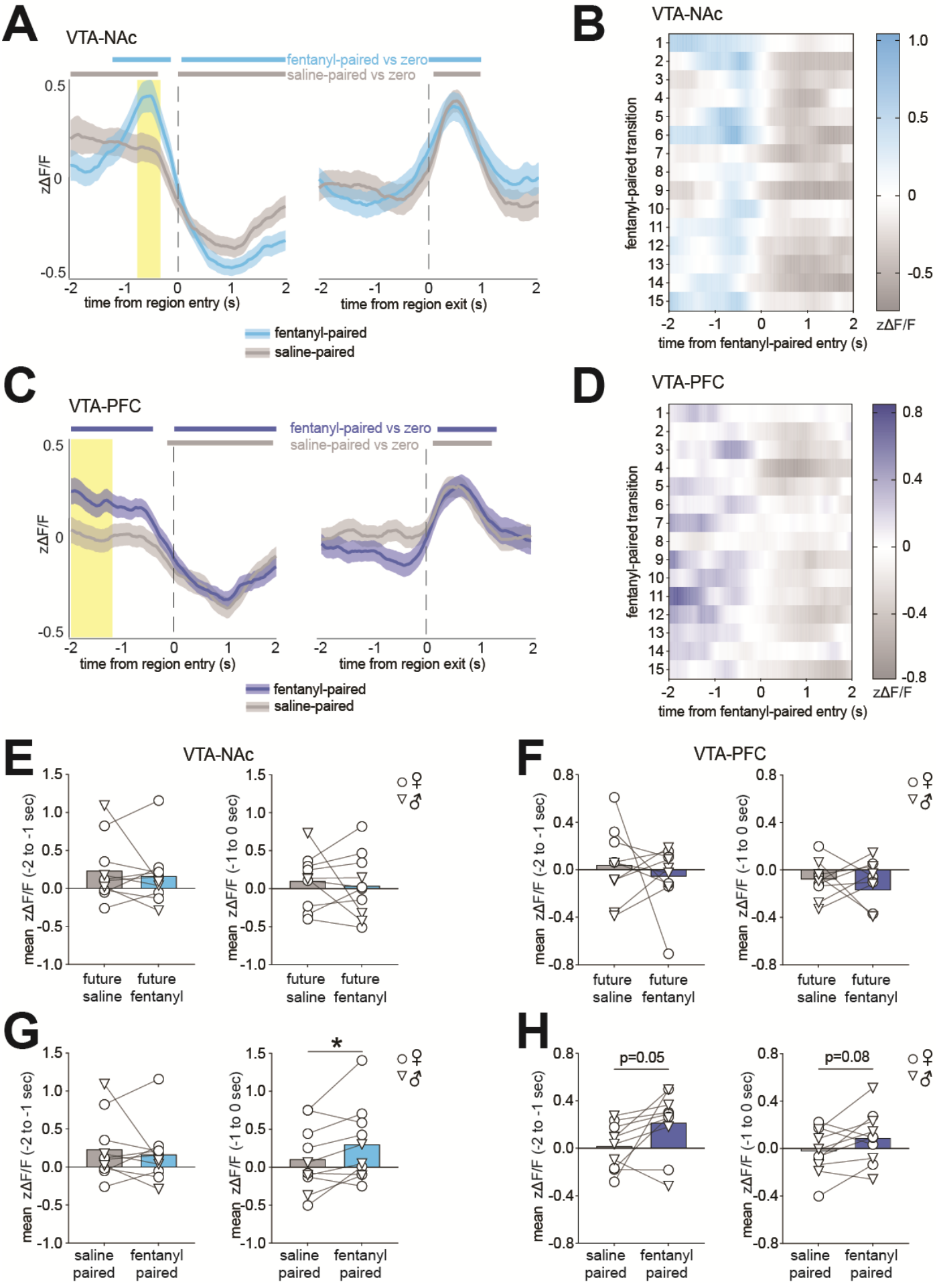
A
VTA-NAc
fentanyl-paired vs zero
saline-paired vs zero
zΔF/F
time from region entry (s)
time from region exit (s)
fentanyl-paired
saline-paired
B
VTA-NAc
fentanyl-paired transition
time from fentanyl-paired entry (s)
zΔF/F
C
VTA-PFC
fentanyl-paired vs zero
saline-paired vs zero
zΔF/F
time from region entry (s)
time from region exit (s)
fentanyl-paired
saline-paired
D
VTA-PFC
fentanyl-paired transition
time from fentanyl-paired entry (s)
zΔF/F
E
VTA-NAc
mean zΔF/F (-2 to -1 sec)
mean zΔF/F (-1 to 0 sec)
future saline
future fentanyl
F
VTA-PFC
mean zΔF/F (-2 to -1 sec)
mean zΔF/F (-1 to 0 sec)
future saline
future fentanyl
G
mean zΔF/F (-2 to -1 sec)
mean zΔF/F (-1 to 0 sec)
*
saline paired
fentanyl paired
H
p=0.05
p=0.08
mean zΔF/F (-2 to -1 sec)
mean zΔF/F (-1 to 0 sec)
saline paired
fentanyl paired

Figure 4. Temporally distinct calcium dynamics of VTA-NAc and VTA-PFC during fentanyl place preference. (**A**) Average zΔF/F for all VTA-NAc mice for 4 seconds surrounding the first 15 entries (left) or exits (right) to the saline-paired (gray trace) or fentanyl-paired (blue trace) context. Vertical dotted line represents the time of entry/exit. Using bootstrapped 95% confidence intervals, gray and blue horizontal bars represent where the gray and blue traces (saline-paired and fentanyl-paired, respectively) significantly differ from 0, and yellow shaded area represents where the two traces significantly differ from one another. (**B**) Heatmap of VTA-NAc activity for the 4 seconds surrounding the first 15 entries into the fentanyl-paired region. Color represents zΔF/F averaged across all VTA-NAc mice. (**C-D**) Same as A-B, but for VTA-PFC. During the pre-test for (**E**) VTA-NAc and (**F**) VTA-PFC, there is no difference in mean zΔF/F from -2 to -1 seconds (left) or -1 to 0 seconds (right) preceding entry to either context. (**G**) During the post-test for VTA-NAc, there is greater calcium activity from -1 to 0 second preceding entries to fentanyl-paired vs saline-paired context (n=10; *, p=0.04). (**H**) During post-test for VTA-PFC, there is a trend towards increased mean zΔF/F during entries to fentanyl-paired context at both -2 to -1, and -1 to 0 (n=10). Circles represent data points from females and triangles represent data points from males.

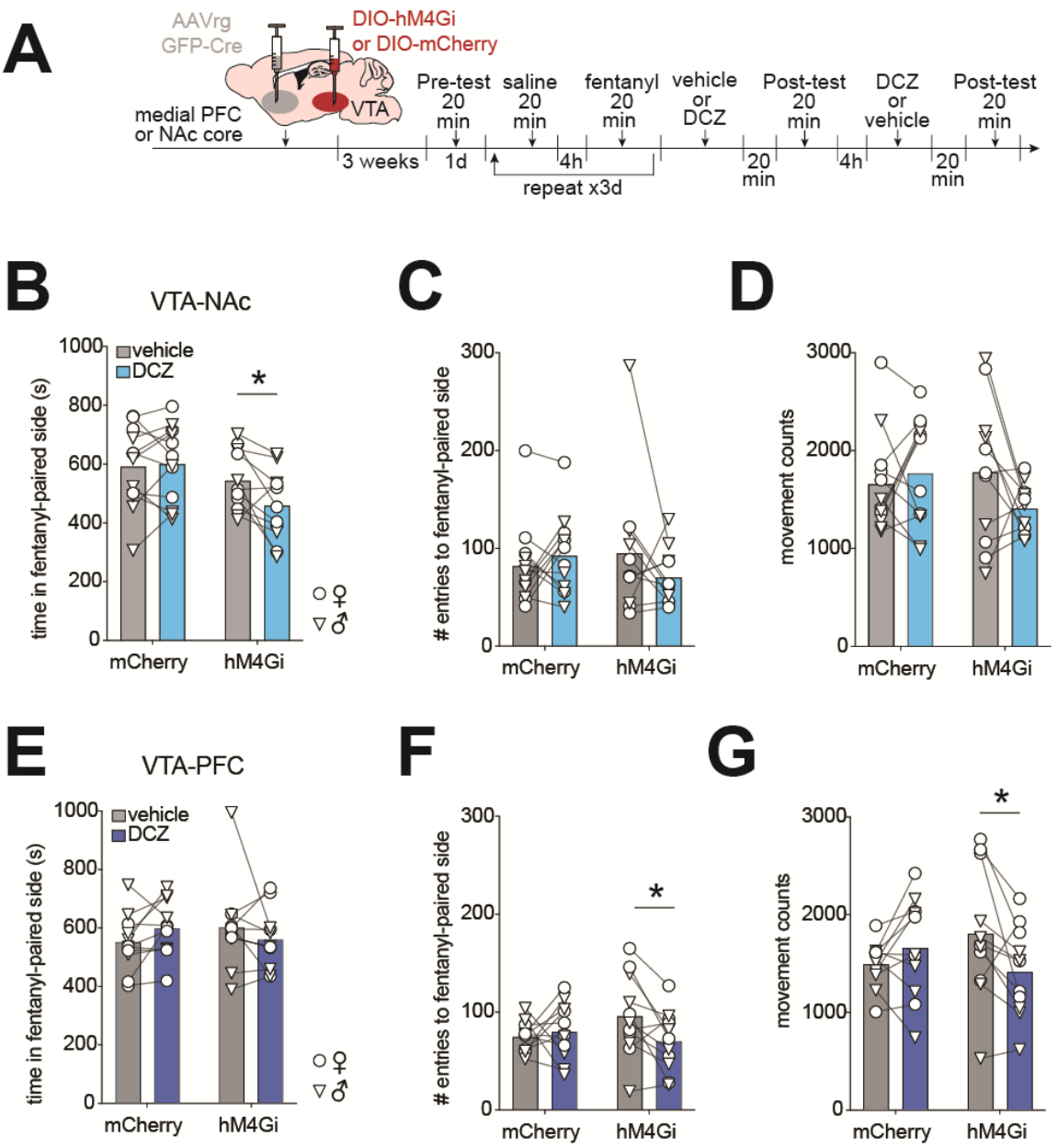

Figure 5. Chemogenetic inhibition of VTA-NAc vs VTA-PFC differentially impacts fentanyl place preference. (**A**) Timeline for chemogenetic experiments. Mice received retrograde-Cre in either medial PFC or NAc core, and Cre-dependent hM4Gi, or Cre-dependent mCherry, in VTA. Twenty minutes prior to each post-test, mice received DCZ (0.1 mg/kg i.p.) or vehicle in a counterbalanced repeated-measures design. (**B**) Time spent in fentanyl-paired context (*, p=0.012), (**C**) number of entries to fentanyl-paired context, and (**D**) total movement counts after treatment with vehicle (gray) and DCZ (light blue) in mice expressing mCherry or hM4Gi in VTA-NAc. (**E**) Time spent in fentanyl-paired context, (**F**) number of entries to fentanyl-paired context (*, p=0.046), and (**G**) total movement counts (*, p=0.028) after treatment with vehicle (gray) and DCZ (dark blue) in mice expressing mCherry or hM4Gi in VTA-PFC. Circles represent data points from females and triangles represent data points from males. N=11-12 per group.

References

1. Spencer MR, Garnett MF, Miniño AM. Drug Overdose Deaths in the United States, 2002–2022. NCHS Data Brief, No 491. 2024;Hyattsville, MD: National Center for Health Statistics.
2. Kelly E, Sutcliffe K, Cavallo D, Ramos-Gonzalez N, Alhosan N, Henderson G. The anomalous pharmacology of fentanyl. British J Pharmacology. 2023;180:797–812.
3. Sutcliffe KJ, Corey RA, Alhosan N, Cavallo D, Groom S, Santiago M, et al. Interaction With the Lipid Membrane Influences Fentanyl Pharmacology. Adv Drug Alcohol Res. 2022;2:10280.
4. Eshleman AJ, Nagarajan S, Wolfrum KM, Reed JF, Nilsen A, Torralva R, et al. Affinity, potency, efficacy, selectivity, and molecular modeling of substituted fentanyls at opioid receptors. Biochemical Pharmacology. 2020;182:114293.
5. Socias ME, Wood E, Le Foll B, Lim R, Choi JC, Mok WY, et al. Impact of fentanyl use on initiation and discontinuation of methadone and buprenorphine/naloxone among people with prescription-type opioid use disorder: secondary analysis of a Canadian treatment trial. Addiction. 2022;117:2662–2672.
6. Koob GF, Volkow ND. Neurocircuitry of Addiction. Neuropsychopharmacol. 2010;35:217–238.
7. Doyle MA, Mazei-Robison MS. Opioid-Induced Molecular and Cellular Plasticity of Ventral Tegmental Area Dopamine Neurons. Cold Spring Harb Perspect Med. 2021;11:a039362.
8. Bozarth MA, Wise RA. Intracranial self-administration of morphine into the ventral tegmental area in rats. Life Sciences. 1981;28:551–555.
9. Van Ree JM, De Wied D. Involvement of neurohypophyseal peptides in drug-mediated adaptive responses. Pharmacology Biochemistry and Behavior. 1980;13:257–263.
10. Lammel S, Hetzel A, Häckel O, Jones I, Liss B, Roeper J. Unique Properties of Mesoprefrontal Neurons within a Dual Mesocorticolimbic Dopamine System. Neuron. 2008;57:760–773.
11. Margolis EB, Mitchell JM, Ishikawa J, Hjelmstad GO, Fields HL. Midbrain Dopamine Neurons: Projection Target Determines Action Potential Duration and Dopamine D_2 Receptor Inhibition. J Neurosci. 2008;28:8908–8913.
12. Beier KT, Steinberg EE, DeLoach KE, Xie S, Miyamichi K, Schwarz L, et al. Circuit Architecture of VTA Dopamine Neurons Revealed by Systematic Input-Output Mapping. Cell. 2015;162:622–634.
13. Elum JE, Szelenyi ER, Juarez B, Murry AD, Loginov G, Zamorano CA, et al. Distinct dynamics and intrinsic properties in ventral tegmental area populations mediate reward association and motivation. Cell Reports. 2024;43:114668.
14. Chaudhury D, Walsh JJ, Friedman AK, Juarez B, Ku SM, Koo JW, et al. Rapid regulation of depression-related behaviours by control of midbrain dopamine neurons. Nature. 2013;493:532–536.
15. Friedman AK, Walsh JJ, Juarez B, Ku SM, Chaudhury D, Wang J, et al. Enhancing Depression Mechanisms in Midbrain Dopamine Neurons Achieves Homeostatic Resilience. Science. 2014;344:313–319.
16. Juarez B, Han M-H. Diversity of Dopaminergic Neural Circuits in Response to Drug Exposure. Neuropsychopharmacol. 2016;41:2424–2446.
17. Lewis DA, Melchitzky DS, Sesack SR, Whitehead RE, Sungyoung Auh, Sampson A. Dopamine transporter immunoreactivity in monkey cerebral cortex: Regional, laminar, and ultrastructural localization. J of Comparative Neurology. 2001;432:119–136.
18. Sesack SR, Hawrylak VA, Matus C, Guido MA, Levey AI. Dopamine Axon Varicosities in the Prelimbic Division of the Rat Prefrontal Cortex Exhibit Sparse Immunoreactivity for the Dopamine Transporter. J Neurosci. 1998;18:2697–2708.
19. Morison SL, Doster LB, Vigotsky AD, Centeno MV, Lopez Gonzalez Del Rey N, Apkarian AV, et al. Recruitment of specific dopamine neuron sub-circuits by opioids. Addiction Neuroscience. 2025;17:100233.
20. Simmons SC, Wheeler K, Mazei-Robison MS. Determination of circuit-specific morphological adaptations in ventral tegmental area dopamine neurons by chronic morphine. Mol Brain. 2019;12:10.
21. Margolis EB, Lock H, Chefer VI, Shippenberg TS, Hjelmstad GO, Fields HL. κ opioids selectively control dopaminergic neurons projecting to the prefrontal cortex. Proc Natl Acad Sci USA. 2006;103:2938–2942.
22. Phillips RA, Tuscher JJ, Black SL, Andraka E, Fitzgerald ND, Ianov L, et al. An atlas of transcriptionally defined cell populations in the rat ventral tegmental area. Cell Reports. 2022;39:110616.
23. Fox ME, Montemarano A, Ostman AE, Basu M, Herb B, Ament SA, et al. Transcriptional signatures of fentanyl use in the mouse ventral tegmental area. Addiction Biology. 2024;29:e13403.

24. Fitzgerald ND, Day JJ. Neuronal heterogeneity in the ventral tegmental area: Distinct contributions to reward circuitry and motivated behavior. Addiction Neuroscience. 2025;14:100191.
25. Taylor SR, Badurek S, Dileone RJ, Nashmi R, Minichiello L, Picciotto MR. GABAergic and glutamatergic efferents of the mouse ventral tegmental area. J of Comparative Neurology. 2014;522:3308–3334.
26. Breton JM, Charbit AR, Snyder BJ, Fong PTK, Dias EV, Himmels P, et al. Relative contributions and mapping of ventral tegmental area dopamine and GABA neurons by projection target in the rat. J of Comparative Neurology. 2019;527:916–941.
27. Root DH, Mejias-Aponte CA, Qi J, Morales M. Role of Glutamatergic Projections from Ventral Tegmental Area to Lateral Habenula in Aversive Conditioning. J Neurosci. 2014;34:13906–13910.
28. Wang H-L, Qi J, Zhang S, Wang H, Morales M. Rewarding Effects of Optical Stimulation of Ventral Tegmental Area Glutamatergic Neurons. J Neurosci. 2015;35:15948–15954.
29. McGovern DJ, Polter AM, Root DH. Neurochemical Signaling of Reward and Aversion to Ventral Tegmental Area Glutamate Neurons. J Neurosci. 2021;41:5471–5486.
30. Zell V, Steinkellner T, Hollon NG, Warlow SM, Souter E, Faget L, et al. VTA Glutamate Neuron Activity Drives Positive Reinforcement Absent Dopamine Co-release. Neuron. 2020;107:864-873.e4.
31. van Zessen R, Phillips JL, Budygin EA, Stuber GD. Activation of VTA GABA Neurons Disrupts Reward Consumption. Neuron. 2012;73:1184–1194.
32. Tan KR, Yvon C, Turiault M, Mirzabekov JJ, Doehner J, Labouèbe G, et al. GABA Neurons of the VTA Drive Conditioned Place Aversion. Neuron. 2012;73:1173–1183.
33. Warlow SM, Singhal SM, Hollon NG, Faget L, Dowlat DS, Zell V, et al. Mesoaccumbal glutamate neurons drive reward via glutamate release but aversion via dopamine co-release. Neuron. 2024;112:488-499.e5.
34. Root DH, Barker DJ, Estrin DJ, Miranda-Barrientos JA, Liu B, Zhang S, et al. Distinct Signaling by Ventral Tegmental Area Glutamate, GABA, and Combinatorial Glutamate-GABA Neurons in Motivated Behavior. Cell Reports. 2020;32:108094.
35. Yoo JH, Zell V, Gutierrez-Reed N, Wu J, Ressler R, Shenasa MA, et al. Ventral tegmental area glutamate neurons co-release GABA and promote positive reinforcement. Nat Commun. 2016;7:13697.
36. Oriol L, Chao M, Kollman GJ, Dowlat DS, Singhal SM, Steinkellner T, et al. Ventral tegmental area interneurons revisited: GABA and glutamate projection neurons make local synapses. eLife. 2025;13:RP100085.
37. Bossert JM, Liu SY, Lu L, Shaham Y. A Role of Ventral Tegmental Area Glutamate in Contextual Cue-Induced Relapse to Heroin Seeking. J Neurosci. 2004;24:10726–10730.
38. McGovern DJ, Polter AM, Prévost ED, Ly A, McNulty CJ, Rubinstein B, et al. Ventral tegmental area glutamate neurons establish a mu-opioid receptor gated circuit to mesolimbic dopamine neurons and regulate opioid-seeking behavior. Neuropsychopharmacol. 2023;48:1889–1900.
39. Stuber GD, Hnasko TS, Britt JP, Edwards RH, Bonci A. Dopaminergic Terminals in the Nucleus Accumbens But Not the Dorsal Striatum Corelease Glutamate. Journal of Neuroscience. 2010;30:8229–8233.
40. Lammel S, Steinberg EE, Földy C, Wall NR, Beier K, Luo L, et al. Diversity of Transgenic Mouse Models for Selective Targeting of Midbrain Dopamine Neurons. Neuron. 2015;85:429–438.
41. Root DH, Mejias-Aponte CA, Zhang S, Wang H-L, Hoffman AF, Lupica CR, et al. Single rodent mesohabenular axons release glutamate and GABA. Nat Neurosci. 2014;17:1543–1551.
42. Holly EN, Miczek KA. Ventral tegmental area dopamine revisited: effects of acute and repeated stress. Psychopharmacology. 2016;233:163–186.
43. Wang F, Liu C, Wang Y, Wang X, Yang Y, Jiang C, et al. Morphine- and foot shock-responsive neuronal ensembles in the VTA possess different connectivity and biased GPCR signaling pathway. Theranostics. 2024;14:1126–1146.
44. Koutlas I, Patrikiou L, Van Der Starre SE, Danko D, Wolterink-Donselaar IG, Luijendijk MCM, et al. Distinct ventral tegmental area neuronal ensembles are indispensable for reward-driven approach and stress-driven avoidance behaviors. 2024.
45. Montemarano A, Fox LD, Alkhaleel FA, Ostman AE, Sohail H, Pandey S, et al. A Drd1-cre mouse line with nucleus accumbens gene dysregulation exhibits blunted fentanyl seeking. 2025.
46. Sherathiya VN, Schaid MD, Seiler JL, Lopez GC, Lerner TN. GuPPy, a Python toolbox for the analysis of fiber photometry data. Sci Rep. 2021;11:24212.
47. Jean-Richard-dit-Bressel P, Clifford CWG, McNally GP. Analyzing Event-Related Transients: Confidence Intervals, Permutation Tests, and Consecutive Thresholds. Front Mol Neurosci. 2020;13:14.

48. Fox ME, Chandra R, Menken MS, Larkin EJ, Nam H, Engeln M, et al. Dendritic remodeling of D1 neurons by RhoA/Rho-kinase mediates depression-like behavior. Mol Psychiatry. 2020;25:1022–1034.
49. Fox ME, Wulff AB, Franco D, Choi EY, Calarco CA, Engeln M, et al. Adaptations in Nucleus Accumbens Neuron Subtypes Mediate Negative Affective Behaviors in Fentanyl Abstinence. Biological Psychiatry. 2023;93:489–501.
50. Smith T, Heger A, Sudbery I. UMI-tools: modeling sequencing errors in Unique Molecular Identifiers to improve quantification accuracy. Genome Res. 2017;27:491–499.
51. Dobin A, Davis CA, Schlesinger F, Drenkow J, Zaleski C, Jha S, et al. STAR: ultrafast universal RNA-seq aligner. Bioinformatics. 2013;29:15–21.
52. Liao Y, Smyth GK, Shi W. featureCounts: an efficient general purpose program for assigning sequence reads to genomic features. Bioinformatics. 2014;30:923–930.
53. Ritchie ME, Phipson B, Wu D, Hu Y, Law CW, Shi W, et al. limma powers differential expression analyses for RNA-sequencing and microarray studies. Nucleic Acids Research. 2015;43:e47–e47.
54. Cahill KM, Huo Z, Tseng GC, Logan RW, Seney ML. Improved identification of concordant and discordant gene expression signatures using an updated rank-rank hypergeometric overlap approach. Sci Rep. 2018;8:9588.
55. Kolberg L, Raudvere U, Kuzmin I, Vilo J, Peterson H. gprofiler2 -- an R package for gene list functional enrichment analysis and namespace conversion toolset g:Profiler. F1000Research. 2020;9.
56. Janky R, Verfaillie A, Imrichová H, Van De Sande B, Standaert L, Christiaens V, et al. iRegulon: From a Gene List to a Gene Regulatory Network Using Large Motif and Track Collections. PLoS Comput Biol. 2014;10:e1003731.
57. Uddin O, Jenne C, Fox ME, Arakawa K, Keller A, Cramer N. Divergent profiles of fentanyl withdrawal and associated pain in mice and rats. Pharmacology Biochemistry and Behavior. 2021;200:173077.
58. Heymann G, Jo YS, Reichard KL, McFarland N, Chavkin C, Palmiter RD, et al. Synergy of Distinct Dopamine Projection Populations in Behavioral Reinforcement. Neuron. 2020;105:909-920.e5.
59. Plaisier SB, Taschereau R, Wong JA, Graeber TG. Rank–rank hypergeometric overlap: identification of statistically significant overlap between gene-expression signatures. Nucleic Acids Research. 2010;38:e169–e169.
60. Robison AJ, Nestler EJ. Transcriptional and epigenetic mechanisms of addiction. Nat Rev Neurosci. 2011;12:623–637.
61. Bali P, Kenny PJ. Transcriptional mechanisms of drug addiction. Dialogues in Clinical Neuroscience. 2019;21:379–387.
62. Calipari ES, Juarez B, Morel C, Walker DM, Cahill ME, Ribeiro E, et al. Dopaminergic dynamics underlying sex-specific cocaine reward. Nat Commun. 2017;8:13877.
63. Xu Y-T, Robson MJ, Szeszel-Fedorowicz W, Patel D, Rooney R, McCurdy CR, et al. CM156, a sigma receptor ligand, reverses cocaine-induced place conditioning and transcriptional responses in the brain. Pharmacology Biochemistry and Behavior. 2012;101:174–180.
64. Feng J, Wilkinson M, Liu X, Purushothaman I, Ferguson D, Vialou V, et al. Chronic cocaine-regulated epigenomic changes in mouse nucleus accumbens. Genome Biol. 2014;15:R65.
65. Navandar M, Martín-García E, Maldonado R, Lutz B, Gerber S, Ruiz De Azua I. Transcriptional signatures in prefrontal cortex confer vulnerability versus resilience to food and cocaine addiction-like behavior. Sci Rep. 2021;11:9076.
66. Winstanley CA, LaPlant Q, Theobald DEH, Green TA, Bachtell RK, Perrotti LI, et al. ΔFosB Induction in Orbitofrontal Cortex Mediates Tolerance to Cocaine-Induced Cognitive Dysfunction. J Neurosci. 2007;27:10497–10507.
67. Wang Y, Singh A, Li G, Yue S, Hertel K, Wang Z-J. Opioid induces increased DNA damage in prefrontal cortex and nucleus accumbens. Pharmacology Biochemistry and Behavior. 2023;224:173535.
68. Castel J, Li G, Onimus O, Leishman E, Cani PD, Bradshaw H, et al. NAPE-PLD in the ventral tegmental area regulates reward events, feeding and energy homeostasis. Mol Psychiatry. 2024;29:1478–1490.
69. Fotio Y, Ciccocioppo R, Piomelli D. N-acylethanolamine acid amidase (NAAA) inhibition decreases the motivation for alcohol in Marchigian Sardinian alcohol-preferring rats. Psychopharmacology. 2021;238:249–258.
70. Lane DA, Lessard AA, Chan J, Colago EEO, Zhou Y, Schlussman SD, et al. Region-Specific Changes in the Subcellular Distribution of AMPA Receptor GluR1 Subunit in the Rat Ventral Tegmental Area after Acute or Chronic Morphine Administration. J Neurosci. 2008;28:9670–9681.

71. Yan Y, Peng C, Arvin MC, Jin X-T, Kim VJ, Ramsey MD, et al. Nicotinic Cholinergic Receptors in VTA Glutamate Neurons Modulate Excitatory Transmission. Cell Reports. 2018;23:2236–2244.
72. Li X, Xiong J, Zhang B, Zhangsun D, Luo S. α-Conotoxin TxIB Inhibits Development of Morphine-Induced Conditioned Place Preference in Mice via Blocking α6β2* Nicotinic Acetylcholine Receptors. Front Pharmacol. 2021;12:772990.
73. Dautan D, Souza AS, Huerta-Ocampo I, Valencia M, Assous M, Witten IB, et al. Segregated cholinergic transmission modulates dopamine neurons integrated in distinct functional circuits. Nat Neurosci. 2016;19:1025–1033.
74. Pulipparacharuvil S, Renthal W, Hale CF, Taniguchi M, Xiao G, Kumar A, et al. Cocaine Regulates MEF2 to Control Synaptic and Behavioral Plasticity. Neuron. 2008;59:621–633.
75. Dieterich A, Floeder J, Stech K, Lee J, Srivastava P, Barker DJ, et al. Activation of Basolateral Amygdala to Nucleus Accumbens Projection Neurons Attenuates Chronic Corticosterone-Induced Behavioral Deficits in Male Mice. Front Behav Neurosci. 2021;15:643272.
76. Larson EB, Graham DL, Arzaga RR, Buzin N, Webb J, Green TA, et al. Overexpression of CREB in the Nucleus Accumbens Shell Increases Cocaine Reinforcement in Self-Administering Rats. J Neurosci. 2011;31:16447–16457.
77. Carlezon WA, Thome J, Olson VG, Lane-Ladd SB, Brodkin ES, Hiroi N, et al. Regulation of Cocaine Reward by CREB. Science. 1998;282:2272–2275.
78. Brunzell DH, Mineur YS, Neve RL, Picciotto MR. Nucleus Accumbens CREB Activity is Necessary for Nicotine Conditioned Place Preference. Neuropsychopharmacol. 2009;34:1993–2001.
79. Misra K, Roy A, Pandey SC. Effects of voluntary ethanol intake on the expression of Ca2+/calmodulin-dependent protein kinase IV and on CREB expression and phosphorylation in the rat nucleus accumbens: Neuroreport. 2001;12:4133–4137.
80. Guitart X, Thompson MA, Mirante CK, Greenberg ME, Nestler EJ. Regulation of Cyclic AMP Response Element-Binding Protein (CREB) Phosphorylation by Acute and Chronic Morphine in the Rat Locus Coeruleus. Journal of Neurochemistry. 1992;58:1168–1171.
81. Nestler EJ, Tallman JF. Chronic morphine treatment increases cyclic AMP-dependent protein kinase activity in the rat locus coeruleus. Molecular Pharmacology. 1988;33:127–132.
82. Widnell KL, Self DW, Lane SB, Russell DS, Vaidya VA, Miserendino MJ, et al. Regulation of CREB expression: in vivo evidence for a functional role in morphine action in the nucleus accumbens. J Pharmacol Exp Ther. 1996;276:306–315.
83. Tervo DGR, Hwang B-Y, Viswanathan S, Gaj T, Lavzin M, Ritola KD, et al. A Designer AAV Variant Permits Efficient Retrograde Access to Projection Neurons. Neuron. 2016;92:372–382.
84. Shinohara F, Kamii H, Minami M, Kaneda K. The Role of Dopaminergic Signaling in the Medial Prefrontal Cortex for the Expression of Cocaine-Induced Conditioned Place Preference in Rats. Biological & Pharmaceutical Bulletin. 2017;40:1983–1989.
85. Hiroi N, White NM. The amphetamine conditioned place preference: differential involvement of dopamine receptor subtypes and two dopaminergic terminal areas. Brain Research. 1991;552:141–152.
86. O'Neal TJ, Bernstein MX, MacDougall DJ, Ferguson SM. A Conditioned Place Preference for Heroin Is Signaled by Increased Dopamine and Direct Pathway Activity and Decreased Indirect Pathway Activity in the Nucleus Accumbens. J Neurosci. 2022;42:2011–2024.
87. Hnasko TS, Sotak BN, Palmiter RD. Morphine reward in dopamine-deficient mice. Nature. 2005;438:854–857.
88. Hnasko TS, Sotak BN, Palmiter RD. Cocaine-Conditioned Place Preference by Dopamine-Deficient Mice Is Mediated by Serotonin. J Neurosci. 2007;27:12484–12488.
89. Reeves KC, Kube MJ, Grecco GG, Fritz BM, Muñoz B, Yin F, et al. Mu opioid receptors on vGluT2-expressing glutamatergic neurons modulate opioid reward. Addiction Biology. 2021;26:e12942.